




Three-dimensional imaging of grain boundaries via quantitative fluorescence X-ray tomography analysis

Mingyuan Ge¹, Xiaojing Huang¹, Hanfei Yan ¹, Doga Gursoy ², Yuqing Meng³, Jiayong Zhang¹, Sanjit Ghose¹, Wilson K. S. Chiu⁴, Kyle S. Brinkman ³ & Yong S. Chu¹✉

Three-dimensional visualization of material composition within multiple grains and across complex networks of grain boundaries at nanoscales can provide new insight into the structure evolution and emerging functional properties of the material for diverse applications. Here, using nanoscale scanning X-ray fluorescence tomography, coupled with an advanced self-absorption correction algorithm developed in this work, we analyze the three-dimensional gain distributions and compositions in a $\text{Ce}_{0.8}\text{Gd}_{0.2}\text{O}_{2-6}\text{-CoFe}_2\text{O}_4$ mixed ionic-electronic conductor system with high accuracy and statistical significance. Our systematic investigation reveals an additional emergent phase and uncovers highly intriguing composition stability ranges for the multiple material phases within this system. The presented visualization of composition variations across complex interfaces, supported by our quantitative composition analysis, discloses mechanistic pathways of the diverse phase transformations occurring in the material synthesis, providing insights for the optimization of transport properties in the mixed ionic-electronic conductor system.

¹National Synchrotron Light Source II (NSLS-II), Brookhaven National Laboratory, Upton, NY 11973, USA. ²X-ray Science Division, Argonne National Laboratory, Lemont, IL 60439, USA. ³Department of Materials Science and Engineering, Clemson University, Clemson, SC 29634, USA. ⁴Department of Mechanical Engineering, University of Connecticut, Storrs, CT 06269, USA. ✉email: ychu@bnl.gov

The formation of grain boundaries and physical processes occurring around grain boundaries have a substantial impact on a wide range of material properties^{1–6}. Consequently, achieving robust methods for quantifying the 3D nanostructure of individual grains and their network is a grand challenge for material science. Electron microscopy, such as Transmission Electron Microscopy (TEM), has been the most popular tool since it offers outstanding spatial resolutions and excellent microstructural sensitivity. However, it is not suited for characterizing a large number of grains due to the limited penetration depth of electrons. Though offering sufficient penetration depth, X-ray microscopy techniques face their own challenges. Recent advances in instrumentation and imaging techniques have significantly enhanced the resolution for X-ray microscopy^{7–11}. On the other hand, achieving robust 3D quantification over a large number of grains and grain boundaries is still an open question.

Transmission ptychography¹² is a powerful imaging technique, which provides a spatial resolution beyond the limit of the focusing optics. However, its imaging contrast is limited only to the electronic density, offering no sensitivity to crystalline ordering and indirect sensitivity to elemental distribution. Transmission X-ray microscopy (TXM), with excellent nanoscale imaging throughput, shares similar contrast limitations for imaging grain boundaries. Diffraction-based imaging techniques such as nano-diffraction¹³, Bragg ptychography¹⁴, dark-field microscopy¹⁵, and Differential Aperture X-ray Laue Micro-diffraction (DAXM)¹⁶ offer impressive capabilities for imaging crystalline ordering with their unique advantages. On the other hand, these methods do not offer a straightforward way of quantifying the composition of grains and elemental diffusion within individual grains or across grain boundaries.

X-ray fluorescence (XRF) microscopy, broadly used as a general-purpose imaging tool for heterogeneous materials, provides outstanding sensitivity to elemental^{17–22}. Taking advantage of high-resolution X-ray optics, 3D XRF imaging or XRF nanotomography has been successfully employed to visualize phase separation¹⁹ and corrosion occurring at grain boundaries¹⁸. However, accurate quantification of elemental concentrations from XRF tomography is hampered by a long-standing difficulty, known as the self-absorption problem, in which the emitted fluorescence photons are absorbed in the specimen, making it challenging to quantify 3D elemental concentrations. Since Hogan et al. first derived the physical process of XRF tomography and proposed a simplified attenuation correction method by neglecting the energy dependence of the emission process²³ and later with the addition of linear models of the photoelectric absorption process²⁴, various reconstruction approaches have been developed based on direct inversion²⁵, algebraic reconstruction technique²⁶, conjugate gradient method²⁷, fast numerical inversion²⁴, alternating minimization²⁸, and maximum-likelihood based iterative approach^{29–31}, to solve the inverse problem of attenuated Radon transform. Alternate approaches of using additional imaging modalities have been developed to achieve improved accuracy^{32–34}. Huang et al. quantified elemental distribution in a 2D slice of a fisheye with about 20 μm resolution by accounting for self-absorption but assuming the uniform distribution of the hosting matrix³⁵. Most previous methods have shortcomings because the absorption is corrected only at the incidence beam energy and not at the fluorescence energies of interest. All these previous methods employed an idealized 2D geometry, which is highly inadequate for quantifying actual XRF tomography data, particularly those with complex internal structures. We illustrate the 3D detection geometry in Fig. 1. Proper treatment of the detection geometry is even more critical when the sample consists of multi-phase components with

strong local absorption variations. Here, we develop a method to address the remaining issues as presented in the previous studies. Instead of an idealized 2D geometry, we take the 3D object into account without a compromise to evaluate the attenuation of fluorescence emitted from each element at individual voxel spatially and iteratively correct the self-absorption using maximum-likelihood. Furthermore, our method only requires XRF images for performing the correction without requiring absorption data³². Adopting our approach, we report a quantitative XRF tomography analysis on a multi-component material system with unprecedented details in analyzing phase separation and transformation occurring at grain boundaries of the initial material phases.

Mixed ionic-electronic conductors (MIECs) have found broad applications, including energy conversion^{36,37} and catalysis³⁸. Dual-phase or “composite” MIEC materials consisting of separate ionic and electronic conductive phases offer an attractive solution to tune electrical and mechanical properties in energy conversion systems^{39–44}. Particularly, an MIEC with a $\text{Ce}_{0.8}\text{Gd}_{0.2}\text{O}_{2-x}$ (CGO) oxygen ion conductive phase and a $\text{Co}_{3-x}\text{Fe}_x\text{O}_4$ ($x = 1, 2$) (CFO) electronic conductive phase has received considerable attention due to its excellent conductivity and structural stability^{45–47}. Extensive research has been devoted to engineering the multi-phase structure during high-temperature sintering⁴⁸. Fine-tuning the oxygen vacancy, directly linked to the material composition, plays a crucial role in improving ionic conductivity. Advancement in the research puts a high priority on an accurate characterization of material structure. Using TEM and TXM, Harris et al. observed an emergent phase, termed as GFCCO, formed as individual particles neighboring the CGO and CFO matrix and characterized their 3D microstructure⁴⁵. By investigating their spatial arrangement and spectroscopic features, Lin et al. explained how the emergent phase could avoid phase separation of Gd dopant and promote the conductivity across the grain boundaries among these grains⁴⁶. The formation of the GFCCO phase adjacent to the CGO-CFO grains was confirmed by Ramasamy et al.⁴⁷.

We chose to investigate the CGO-CFO MIEC system for two reasons. First, the XRF imaging has much higher elemental detection sensitivity and can probe a much larger sample volume than electron microscopy methods. Therefore, it is highly likely to discover interesting phase separation or structural transformation that has not been previously reported. Particularly, the earlier reports on the “fixed” elemental composition for the GFCCO phase. For example, in the $\text{Ce}_{0.8}\text{Gd}_{0.2}\text{O}_x\text{-CoFe}_2\text{O}_4$ system, Harris reported an emergent phase in the form of $\text{Gd}_{0.374}\text{Ce}_{0.079}\text{Co}_{0.077}\text{Fe}_{0.47}\text{O}_x$ using EDS mapping in STEM⁴⁵. Using X-ray powder diffraction, Zeng determined it to be $\text{Gd}_{0.85}\text{Ce}_{0.15}\text{Fe}_{0.75}\text{Co}_{0.25}\text{O}_3$ ⁴⁹, and Ramasamy reported a $\text{GdFe}(\text{Ce}, \text{Co})\text{O}_3$ perovskite phase in the $\text{Ce}_{0.8}\text{Gd}_{0.2}\text{O}_x\text{-FeCo}_2\text{O}_4$ system⁴⁷. However, it is unlikely that the emergent phase is formed with a fixed composition considering highly diverse local interfaces with the mother phases. More comprehensive 3D nanoscale imaging is needed for mapping the heterogeneous nature of complex 3D interfaces. Second, the CGO-CFO MIEC system is an excellent model system for XRF absorption correction since it contains multiple high-density phases with significant X-ray absorption. Therefore, if an absorption correction method works on this system, it can also work with other systems with much less structural diversity or lower absorption effects.

In this work, we present the quantitatively analysis of the composition distribution in the CGO-CFO MIEC system using XRF nano tomography, by taking the advantages of the absorption correction approach we have developed. With a survey over 340 grains, we discovered the existence of two emergent phases in the CGO-CFO system and revealed the phase transformation path during the material synthesis.

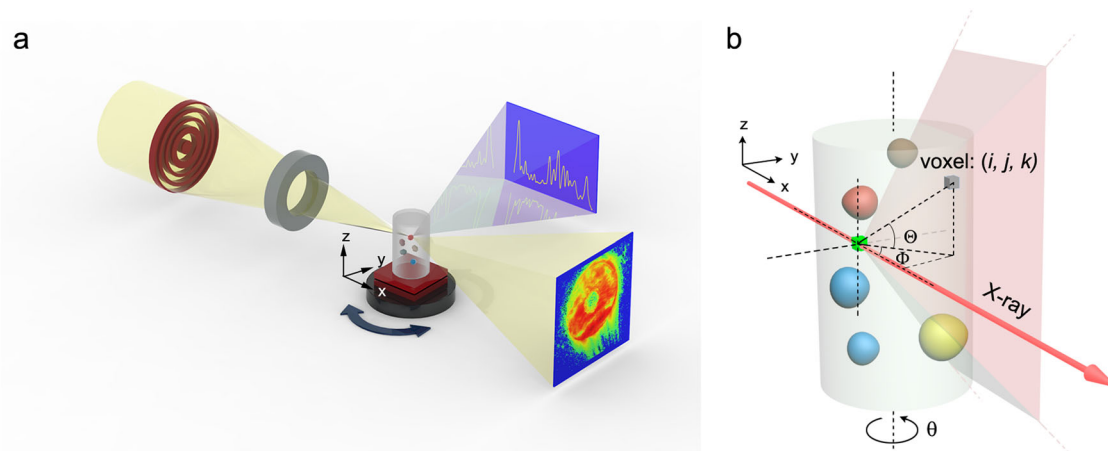


Fig. 1 Fluorescence x-ray tomography setup at the Hard X-ray Nanoprobe at NSLS-II. **a** a monochromatic x-ray beam is focused using a Fresnel zoneplate, together with a central beam stop (not shown) and an order-sorting aperture. The transmitted scattering pattern and fluorescence signals are collected simultaneously. Raster scanning is performed to produce a 2D XRF projection image, and tomography measurement is carried out by collecting a series of 2D XRF images as the sample is rotated about the vertical axis, perpendicular to the x-ray beam. **b** Fluorescence x-rays emitted from an arbitrary point along the incidence x-ray beam, represented by a green voxel. Only a fraction of fluorescence x-rays is captured by a detector with a given solid angle (represented by a pink shape), encoding the absorption through a 3D local region of the sample defined by the detector solid angle (i.e., traversed region). A gray cube represents a voxel within this traversed region, where the absorption is corrected. The traversed region changes with the orientation and position of the sample.

Results and discussion

Absorption correction implementation. The self-absorption effect on the tomography data is easily seen in Fig. 2a. The detected XRF intensity gradually decreases due to the attenuation of the XRF photons, which produces angle-dependent intensity in the sinogram (Fig. 2b) and generates systematic errors in 3D reconstruction (Fig. 2c). The error is more pronounced in the XY slice of the reconstructed volume (Fig. 2d–g and Supplementary Fig. S3a). For example, in Fig. 2d, the Gd intensity of particle S2 is weaker than particle S1. A similar effect is also seen in the reconstructed slices for the other elements.

The physical process of XRF measurement can be described as two distinct events: emission and detection. When passing through the sample, the incidence beam is attenuated along its path before exciting the fluorescence emission. However, only a fraction of the emitted XRF photons is detected due to the self-absorption and limited detection of solid angle. In an XRF tomography scan, the detected XRF intensity at a sample position (θ, ρ) can be described as a set of line integrals of fluorescent emission function, ε , multiplied by a detection function, P , along the incidence beam path L .

$$I(\theta, \rho) = \int_{r \in L(\theta)} \varepsilon(\theta, r) \circ P(\theta, r) dr \quad (1)$$

For the numerical computation of the detected fluorescence intensity, we discretize the emission and detection function using sample voxels (i, j, k) .

$$\varepsilon_{i,j,k}^s(\theta, r) = \sigma^s \cdot C_{i,j,k}^s \cdot I_0 \cdot A_{i,j,k}(\theta, r) \quad (2)$$

In Eq. 2, σ^s denotes the fluorescence cross-section of element s . $C_{i,j,k}^s$ is the concentration of element s . I_0 is a scalar quantity representing the incident beam intensity. $A_{i,j,k}(\theta, r)$ is the attenuation coefficient of the incident beam at voxel (i, j, k) .

The detection function P accounts for the self-absorption experienced by the XRF photons, measured by the detector with a finite solid angle.

$$(\theta, r) = \exp\left(-\Delta l \cdot \sum_{i,j,k} \sum_s \left(C \cdot a^s \cdot m_{i,j,k}^1(\theta, r)\right)\right) \quad (3)$$

In Eq. 3, a^s is the linear attenuation coefficient of element s . Δl is the voxel size. $C = \frac{C_{i,j,k}^s}{\sum_s C_{i,j,k}^s}$ is the concentration fraction of element s . $m_{i,j,k}^1(\theta, r)$ describes the traversed region of the sample for the XRF photon emitted at a position, r . Note that the traversed region varies as a function of the source point of the fluorescence emission. It can be written as,

$$m_{i,j,k}^1(\theta, r) = \begin{cases} 1 / \left[\cos(\Theta_{i,j,k}(\theta, r)) \cdot \cos(\Phi_{i,j,k}(\theta, r)) \right] & \text{voxel}(i, j, k) \text{ inside traversed region} \\ 0 & \text{voxel}(i, j, k) \text{ outside traversed region} \end{cases} \quad (4)$$

In Eq. 4, Φ and Θ are the polar and azimuth angles of the voxels within the traversed region (see Fig. 1b). The numerical value of $\Delta l \cdot m_1$ represents the effective beam path length when the beam travels through the voxel grid. Based on the above equations, the integral in Eq. 1 can be discretized as

$$I(\theta, \rho) = \sum_{i,j,k} \left[m_{i,j,k}^2(\theta, r) \cdot \sigma^s \cdot C_{i,j,k}^s \cdot I_0 \cdot A_{i,j,k}(\theta, r) \cdot \exp\left(-\Delta l \cdot \sum_{i,j,k} \sum_s \left(C \cdot a^s \cdot m_{i,j,k}^1(\theta, r)\right)\right) \right] \quad (5)$$

$$C = \frac{C_{i,j,k}^s}{\sum_s C_{i,j,k}^s} \quad (6)$$

$$m_{i,j,k}^2(\theta, r) = \begin{cases} 1, & (i, j, k) \text{ inside beam path} \\ 0, & (i, j, k) \text{ outside beam path} \end{cases} \quad (7)$$

$m_{i,j,k}^2(\theta, r)$ is a one-dimensional mask function describing the incidence beam path. Equation 5 can be discretized and written as a matrix multiplication (Eq. 8) to facilitate numerical computation, representing the generalized Radon transform⁵⁰. See Supplementary Note 1 for detailed mathematical steps.

$$I(\theta, \rho) = \mathbf{R}(\theta, r) \times \mathbf{C}(r) \quad (8)$$

We use $\mathbf{C}(r)$ to represent the spatially variant material composition. Note that note $\mathbf{R}(\theta, r)$ has an implicit dependence on the elemental concentration. Consequently, the components of $\mathbf{R}(\theta, r)$ and $\mathbf{C}(r)$ cannot be arbitrarily independent. We exploit this inter-dependence using an iterative approach for achieving a self-

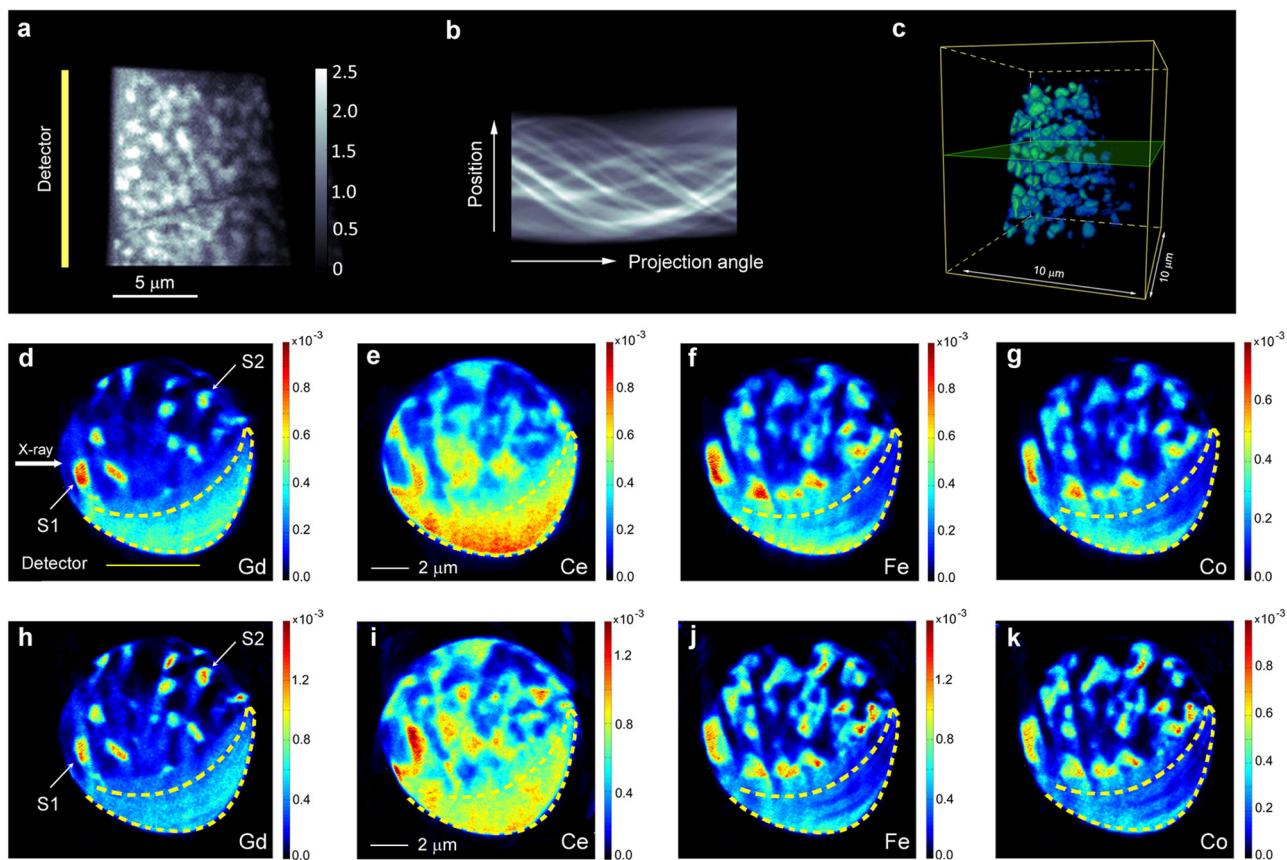


Fig. 2 Comparison of 3D tomography reconstruction without and with absorption correction. **a** 2D fluorescence projection image of Gd. The color bar indicates the relative pixel intensity in the fluorescence image. **b** Sinogram from a single slice of the sample collected -90° to 90° with a 3° interval. Note that the absorption is responsible for a systematic decrease in XRF intensity in **a** and sinogram **b**. **c** reconstructed 3D volume of Gd distribution without correction. **d–g** 2D cross-sectional slice view of 3D elemental distribution for Gd (**d**), Ce (**e**), Fe (**f**), and Co (**g**) without absorption correction. For the sample coordinate used for **d–k** the detector is on the bottom side of the image. **h–k** corresponding 2D slice views after absorption correction. After the absorption correction, the intensity of particles, P1 and P2, became comparable. The dashed region in **d–k** shows the metal redeposition in the FIB process, which is excluded in the quantitative analysis.

consistent solution. We alternatively calculate **C** and **R** by fixing the other until the change in **C** is less than the desired threshold value. Our iterative method often converges after 3–4 iterations, yielding a fast convergence rate. Further technical details are described in Supplementary Note 2, 3, 4.

Element concentration visualization. The outcome of absorption correction is shown in Fig. 2h–k and Supplementary Fig. S3b. After correction, the elemental concentration is more uniformly distributed. For example, we estimate that there is about a 40% change in the Gd concentration after self-absorption correction (Supplementary Fig. S3g). We also observe shaper particle boundaries after correction (Supplementary Fig. S4). This apparent resolution enhancement is achieved by accurately determining voxel values, significantly reducing the boundary-blurring. We will present our quantitative analysis on a total of 340 grains segmented from the whole tomography volume. Note that a small portion of the sample (enclosed by the dotted line in Fig. 2d–g) does not show well-defined individual grains due to aggressive FIB processing. Our following analysis excludes the FIB-affected region of the sample.

Based on the reconstructed XRF intensities, we observed three types of grains: i) Ce-rich (51% volume fraction), ii) Fe/Co-rich (34% volume fraction), and iii) Gd-rich (15% volume fraction). The existence of Ce-rich and Fe/Co-rich grains is originated from the initial materials of CGO and CFO. We refer them to the CGO

phase and CFO phase, respectively, though their actual compositions are significantly modified from the initial bulk values of $\text{Ce}_{0.8}\text{Gd}_{0.2}\text{O}_{1.9}$ and CoFe_2O_4 , respectively. Our discovery of the three grain types is qualitatively consistent with the previous studies^{45–47}. Consequently, the Gd-rich grains correspond to the emergent phase. Also, the X-ray powder diffraction data (Supplementary Note 5, Supplementary Fig. S5) identified three distinctively separate crystalline structures: cubic F-type CeO_2 (ICSD #28796), spinel CoFe_2O_4 (ICSD #39131), and orthorhombic GdFeO_3 or distorted Perovskite (ICSD #27870) crystalline structures, providing further evidence that seems to support the previous studies. However, we discovered that the Gd-rich grains exhibit two distinctive composition ranges among all the 340 grains we had inspected. Consequently, the CGO-CFO MIEC system contains not one but two separate emergent phases. Henceforth, we refer them to EP1 (emergent phase 1) and EP2 (emergent phase 2).

Figure 3a, b show the segmented 3D volume and cross-section view of the sample with all four material phases. Figure 3b clearly shows that both EP1 and EP2 grains are adjacent to the CGO and CFO grains. In Fig. 3c, we display the EP1 and EP2 grains with a grayscale value of $\text{Gd}/(\text{Gd}+\text{Fe})$, which is a highly sensitive parameter to visualize the diffusion of Gd and Fe from their parent phases in the formation of EP1 and EP2. The grains with large Gd fractions belong to the EP1 phase (P1, P2, and P3), and the grains with lower Gd fractions belong to the EP2 phase (some

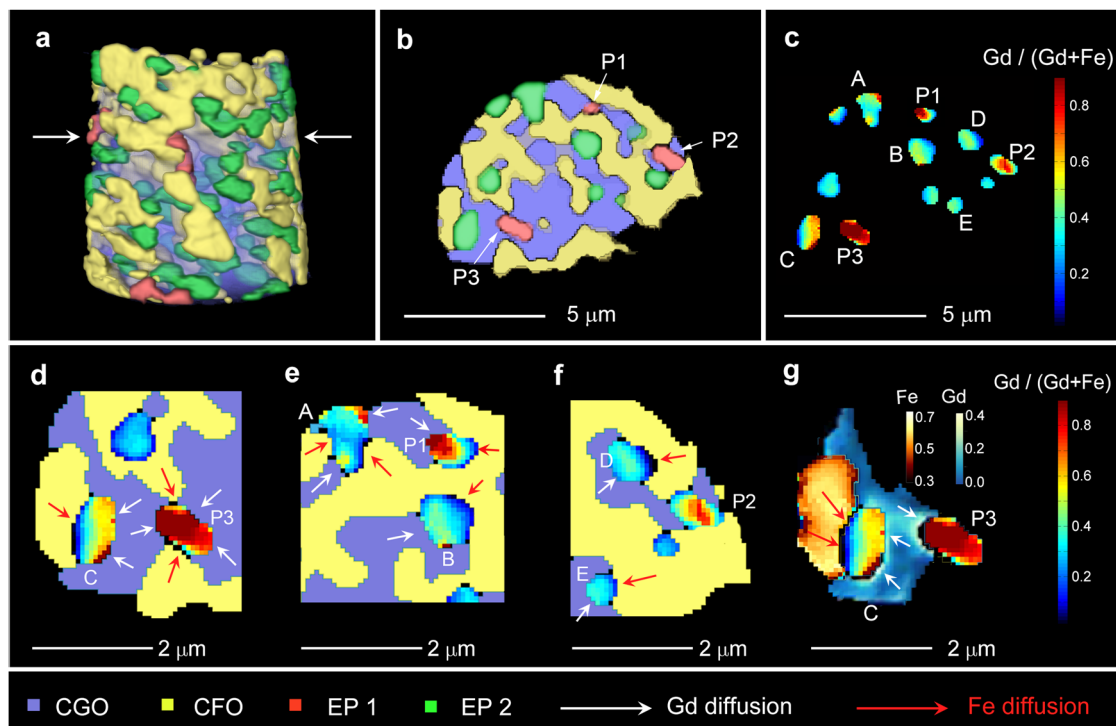


Fig. 3 Visualization of four material phases (CGO, CFO, EP1, and EP2). **a** 3D view of segmented phases. **b** 2D cross-sectional slice through the two arrows shown in **a**. **c** Emergent phases with a grayscale map of $Gd/(Gd+Fe)$ corresponding to the cross-sectional slice in **b**. Note that some grains such as P1 and C exhibit dramatic concentration gradients. **d-f** Enlarged grayscale map of $Gd/(Gd+Fe)$ around EP1 and EP2 grains. White and red arrows indicate the diffusion path for Gd and Fe from the neighboring CGO and CFO phases to emergent phases, EP1 and EP2. **g** Grayscale concentration map of $Gd/(Gd+Fe)$ in the parent phases (CGO and CFO) adjacent to the emergent phase grain C and P3. The Fe color map indicates the Fe concentration in CFO, and the Gd color map shows the Gd concentration in CGO. The parent phases also show higher Gd and Fe local concentrations in the interfacial regions, as indicated by the red and white arrows. Note that for **d-g**, the “rainbow” color scheme adapted from **c** applies to EP1 and EP2 particles only.

of which are labeled as A, B, C, D, E). Take grain A, for example. Its interfacial regions next to the CGO grains show higher Gd fractions, while the local regions bordering the CFO grains show lower Gd fractions, corresponding to higher Fe fractions. The same trend is observed for all grains. To guide the eye, we placed white and red arrows showing the direction of Gd and Fe diffusion from the neighboring grains, respectively (Fig. 3d–g). The emergent phases exhibit significant variation of the Gd fraction value, strongly correlated with their local geometry. Note that grain P3 has a more uniform Gd fraction than others, displaying a snapshot of EP1 grain before receiving significant Fe diffusion.

Statistical grain composition analysis. To perform systematic “Big Data” analysis, we compute the “grain-averaged” metal concentrations and assign quaternary compositions for all 340 grains as described in Methods. Figure 4a displays individual grains on a quaternary phase diagram. Visualization of the quaternary phase diagram at different angles is presented in Supplementary Movie 1. It is fascinating to observe that the composition ranges of the four different phases are highly coordinated and confined in the two compositional planes (see Fig. 4a).

For better visualization and systematic quantification, we projected the quaternary diagram into ternary phase diagrams as described in Method. Four of the most interesting ternary phase diagrams are shown in Fig. 4b–e (see Supplementary Note 6 for details; all 6 phase diagrams can be found in Supplementary Figs. S6 and S7). Investigation of the CGO displays a significant deviation of Ce compared to its nominal concentration in $Gd_{0.2}Ce_{0.8}O_{1.9}$ and an up to 30% Fe

concentration, which suggests a strong atomic interdiffusion across the grain boundaries of the initial two phases (CGO and CFO). In comparison, the CFO phase has a relatively small range of composition distribution from $CoFe_2O_4$. The most interesting finding is that the CGO and EP1 grains exhibit a highly elongated composition spread in the Fe-Co-(Gd+Ce) phase diagram, corresponding to a 2:1 ratio between Fe and Co concentration (i.e. $[Fe]/[Co] = 2$). On the other hand, the composition spread for the EP2 grains is abruptly shifted from the elongated trend of EP1 at ~30% Fe (see the solid line in Fig. 4b) with a very narrow composition range (27% to ~33% Fe) of co-existence, as shown in Fig. 4b, e. It is worth noting that the proper absorption correction is the key to perform quantitative analysis. A comparison of phase diagrams with and without absorption correction can be found in Supplementary Note 7 and Supplementary Fig. S8.

We perform linear fitting analysis to determine the composition of the four material phases, as shown in Fig. 5. The CFO grains have a constant level of Ce concentration with a mean value of 0.01 ± 0.01 (Fig. 5c, d). Using the linear fits of the Gd-Co and Ce-Co data, we determine its metal composition to be $Ce_{0.01}Gd_{0.51-4x/3}Co_xFe_{0.48+x/3}$ for $0.27 < x < 0.37$. Equivalently, the CFO composition can be written in terms of Gd fraction as $Ce_{0.01}Gd_xCo_{0.38-3x/4}Fe_{0.61-x/4}$ for $0.01 < x < 0.14$. The compositions for CGO, EP1, and EP2 are summarized in Fig. 5 and Table 1.

Highly similar compositional behaviors of EP1 and CGO in the Fe-Co-(Gd+Ce) phase diagram strongly suggest that EP1 and CGO have similar crystalline structures. According to the previous studies^{51,52}, the CFO phase with a stoichiometry of $Ce_{1-x}Gd_xO_{2-8}$ maintains the F-type CeO_2 cubic structure with the Gd doping level up to ~30%⁵². A higher level of Gd doping causes the formation of the C-type Gd_2O_3 microdomains growing

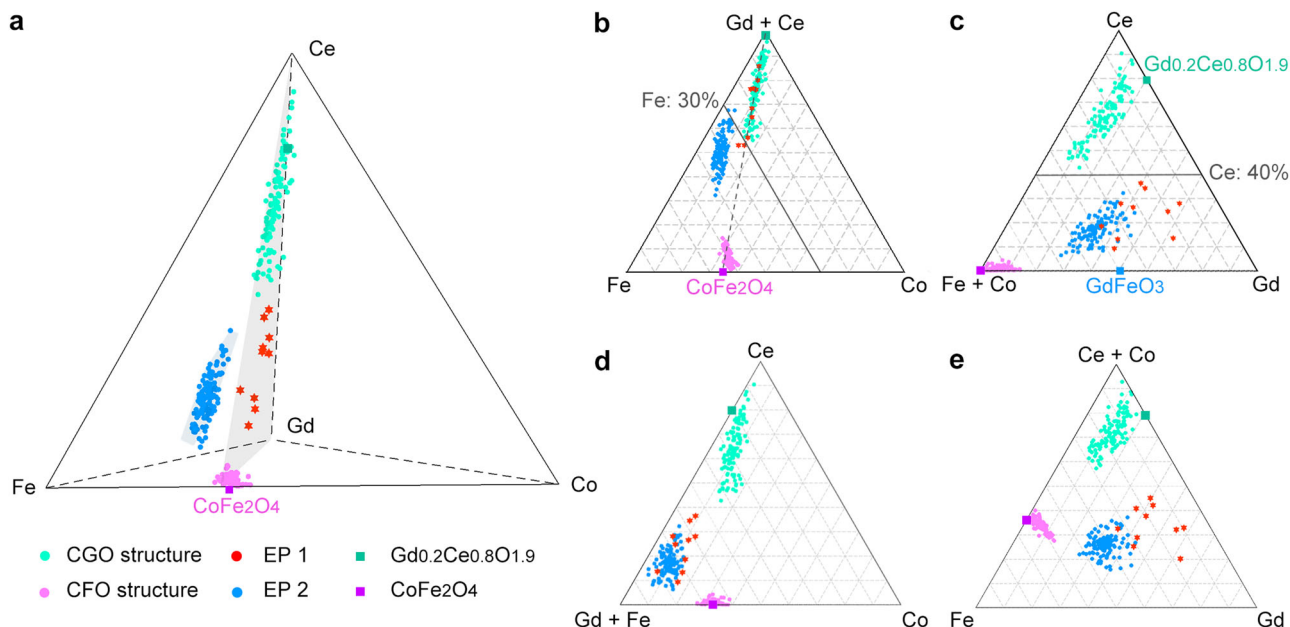


Fig. 4 Composition distribution for four material phases (CGO, CFO, EP1, and EP2). **a** On the quaternary phase diagram. Note that the composition ranges CGO, CFO and EP1 are confined in a single composition plane defined by three points: Ce apex, Gd apex, and the bulk CFO composition value. The composition range of EP2 is categorically displaced from others, restricted to another composition plane that is nearly but not exactly parallel to the plane containing the three phases. **b–e** ternary phase diagrams: Fe-Co-Gd+Ce (**b**), Gd-Ce-(Fe+Co) (**c**), Ce-Co-(Gd+Fe) (**d**), and Gd-Fe-(Ce+Co) (**e**). Only four of all six phase diagrams are shown. See SI for all phase diagrams. As expected, the CFO grains exhibit a small concentration range close to CoFe_2O_4 (represented as a pink square in **b**). The CFO grains display coordination of the Gd and Co concentrations, producing a short elongated compositional streak. The CGO grains exhibit a highly elongated composition spread, aligned with the dotted line in **b**, representing the Fe to Co concentration ratio of 2 ($[\text{Fe}]/[\text{Co}] = 2$). The EP1 grains share an identical Fe-Co compositional relationship as the CGO grains while displaying drastically different Gd and Ce composition ranges (see **c–e**). The EP2 grains exhibit their Fe-Co composition spread, abruptly shifted from the CGO and EP1 grains at ~30% Fe (see solid line in **b**) with very narrow Fe and Gd compositional ranges of co-existence (see **b** and **e**).

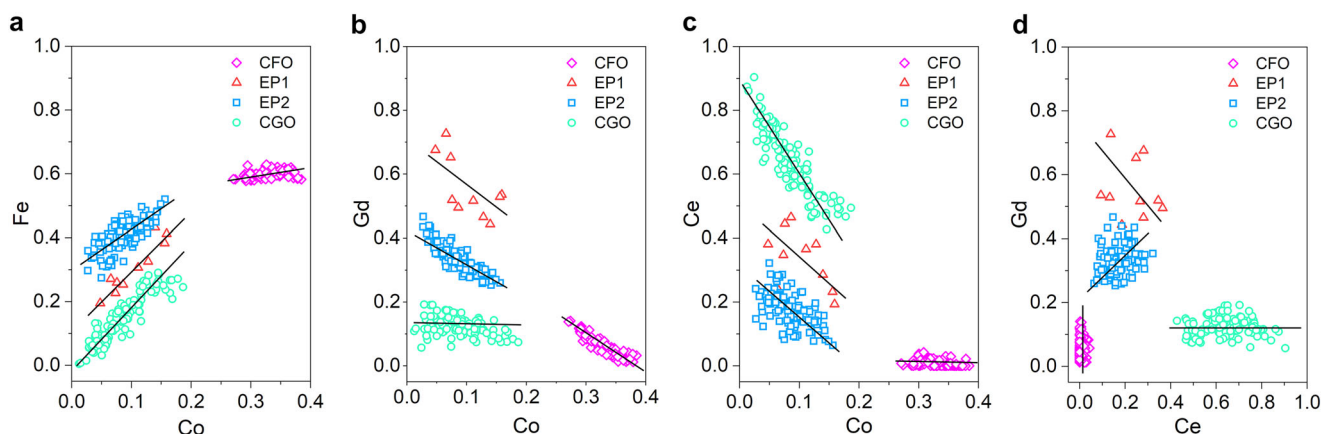


Fig. 5 Linear fitting analysis of the metal concentration to determine the composition of the four material phases in CGO-CFO MIEC system. Fe vs. Co (**a**), Gd vs. Co (**b**), Ce vs. Co (**c**), Gd vs. Ce (**d**). For each panel, the data for EP1 are shifted vertically by 0.1 to provide good data visibility. The solid lines are the linear fits to the data. The following is the summary of the linear fitting results. For CFO, $[\text{Fe}] = 0.48 + [\text{Co}]/3$, $[\text{Gd}] = 0.51 - 4[\text{Co}]/3$, and $[\text{Ce}] = 0.01 \pm 0.01$ for $0.27 < [\text{Co}] < 0.37$. For CGO, $[\text{Fe}] = 2[\text{Co}]$, $[\text{Gd}] = 0.13 \pm 0.13$, and $[\text{Ce}] = 0.88 - 3[\text{Co}]$ for $0 < [\text{Co}] < 0.19$. For EP1, $[\text{Fe}] = 2[\text{Co}]$, $[\text{Gd}] = 0.61 - 3[\text{Co}]/2$, and $[\text{Ce}] = 0.39 - 3[\text{Co}]/2$ for $0.05 < [\text{Co}] < 0.16$. For EP2, $[\text{Fe}] = 0.28 + 3[\text{Co}]/2$, $[\text{Gd}] = 0.42 - [\text{Co}]$, and $[\text{Ce}] = 0.3 - 3[\text{Co}]/2$ for $0.02 < [\text{Co}] < 0.16$. Typical fitting errors are -0.02 for the linear term and -0.03 for the constant term. Determining the composition of EP1 and EP2 is somewhat tricky since EP1 and EP2 do not contain any element with a constant concentration. In addition, the correlation between Gd and Ce is too poor to perform the reliable fitting. By fitting the datasets with better linear correlations (Fe vs. Co, Gd vs. Co, and Ce vs. Co), we deduce the linear trend between Gd and Ce shown in **d**, over which the data points are highly scattered.

coherently within the F-type matrix^{51,52}. The C-type Gd_2O_3 structure is known to exhibit a remarkably similar diffraction pattern as the F-type that is non-trivial to distinguish^{51,52}. In our case, both CGO and EP1 experience much more complex doping of Gd, Fe, and Co, leading to a plausible explanation why these

two structures could not be distinguished using a typical synchrotron powder diffraction, although our measurements have a considerably higher resolution than a laboratory x-ray diffraction. Exhibiting two different metal-to-metal distances (~ 3.6 and ~ 4.1 Å) and three metal-to-oxygen distances (~ 2.2 ,

Table 1 Composition of the four materials phases in the CGO-CFO MIEC system and their crystalline structure.

Material phase	Volume fraction	Composition ranges	Mean Composition	Crystalline Structure
CFO	34%	$\text{Ce}_{0.03} \text{Gd}_{1.51-4x} \text{Co}_{3x} \text{Fe}_{1.44+x} \text{O}_{4.52-1.5x}$ ($0.275 < x < 0.373$)	$\text{Ce}_{0.03} \text{Gd}_{0.23} \text{Co}_{0.97} \text{Fe}_{1.76} \text{O}_{4.03}$	CoFe_2O_4 , spinel
CGO	51%	$\text{Ce}_{0.88-3x} \text{Gd}_{0.12} \text{Co}_x \text{Fe}_{2x} \text{O}_{1.94-2x}$ ($0 < x < 0.19$)	$\text{Ce}_{0.57} \text{Gd}_{0.12} \text{Co}_{0.10} \text{Fe}_{0.2} \text{O}_{1.74}$	CeO_2 , cubic F-type
EP1	2%	$\text{Ce}_{0.78-3x} \text{Gd}_{1.22-3x} \text{Co}_{2x} \text{Fe}_{4x} \text{O}_{3.39-2.5x}$ ($0.05 < x < 0.16$)	$\text{Ce}_{0.47} \text{Gd}_{0.90} \text{Co}_{0.21} \text{Fe}_{0.42} \text{O}_{3.13}$	Gd_2O_3 , cubic C-type
EP2	13%	$\text{Ce}_{0.60-3x} \text{Gd}_{0.82-2x} \text{Co}_{2x} \text{Fe}_{0.56+3x} \text{O}_{3.3-2.5x}$ ($0.02 < x < 0.16$)	$\text{Ce}_{0.33} \text{Gd}_{0.64} \text{Co}_{0.18} \text{Fe}_{0.83} \text{O}_{3.05}$	GdFeO_3 , orthorhombic

The volume fraction of each phase is determined by the segmentation of the volumetric tomography dataset. The quinary compositions defined in the text ($\text{Ce}_w\text{Gd}_x\text{Co}_y\text{Fe}_z$ with $w + x + y + z = 1$) are converted into the conventional bulk compositions based on the crystalline structure of these material phases. The mean composition is taken at the middle of the composition range. The oxygen stoichiometry is estimated by assuming the oxidation states: Ce = 4, Gd = 3, Fe = 3, and Co = 2.

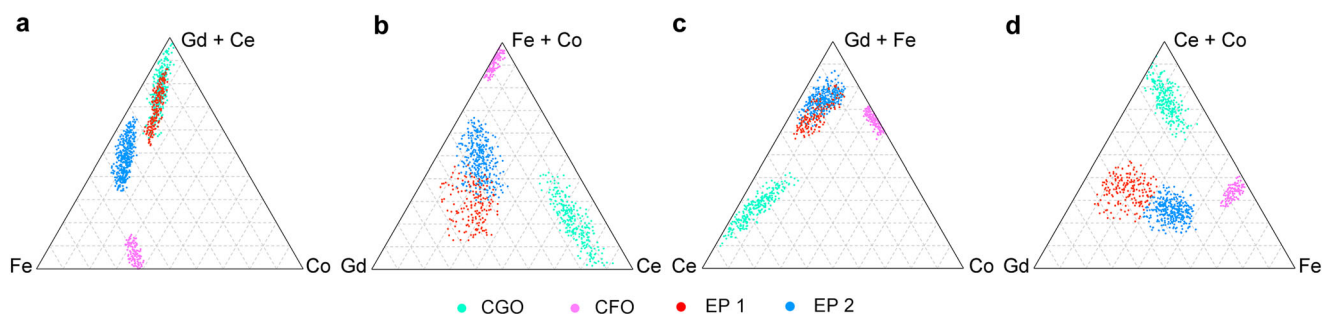


Fig. 6 Simulated ternary phase diagrams. The elemental relationships determined by linear fitting analysis are used to simulate four ternary phase diagrams (**a** Fe-Co-(Gd+Ce); **b** Gd-Ce-(Fe+Co); **c** Ce-Co-(Gd+Fe); **d** Gd-Fe-(Ce+Co)) to be compared with the data in Fig. 4. See Supplementary Fig. S6 and S7 for all 6 phase diagrams.

~ 2.3 , and ~ 2.6 Å), the C-type structure provides greater structural flexibility to accommodate large fractions of metal species of different covalent radii and metal-oxygen bond lengths while minimizing the interfacial strain at the CGO-EP1 grain boundary. On the other hand, the GdFeO_3 structure has an orthorhombic symmetry, making it difficult for the EP2 grains to form structurally coherent interfaces with the CGO and EP1 lattices. Consequently, increasing Fe diffusion into the EP1 lattice would cause an abrupt or the first-order structural phase transformation into EP2. This is a drastic contrast to the structural modification from the CGO to EP1, which exhibits the characteristics of the second-order phase transformation. Alternatively, it could be argued that the EP1 and EP2 phases are formed independently, in such a way that the EP1 phase grains are nucleated in the region adjacent to the CGO phases, while the EP2 grains are formed next to the CFO phases. However, our data do not show significantly different local arrangements between the EP1 and EP2. In addition, if the two phases were formed independently, it would be highly unlikely that they would exhibit a sharp concentration boundary at 30% Fe. Instead, we would expect a more diffused concentration boundary between these two phases. Therefore, this alternate scenario is much less likely. Given that the volume fraction of the EP1 phase is relatively small ($\sim 2\%$) and contains smaller fractions of Fe concentration, it is likely that the EP1 phase may eventually be converted to EP2 phase with a longer sintering time or higher fraction of CFO in the initial mixture.

In order to establish the confidence that the determined quaternary compositions appropriately describe the entire set of data, we present the simulated phase diagrams for all four material phases in Fig. 6. Additional information can be found in Supplementary Note 6. The simulations exhibit excellent agreement with the experimental data, even though our analysis is

based only on the linear trend of the data (Table 1). Though we do not have direct experimental evidence for determining the oxygen concentrations, we estimate the oxygen stoichiometry by assuming the oxidation states of the metal species (Ce=4, Gd=3, Fe=3, and Co=2). Such estimation indicates that EP1, EP2, and CFO phases are fully oxygenated with the oxygen stoichiometry very close to the bulk value, while the CGO phase exhibits considerable oxygen deficiency.

Quantitative analysis of a large number of grains provides an important opportunity for gaining material insight into the mechanistic nature of phase transformation and elemental diffusion. A strong positive correlation between Fe and Co for CGO and EP1 indicates that Fe and Co are diffused together into these phases. In particular, the striking composition spreads of Fe and Co with a ratio of 2:1 further suggests that Fe and Co are diffused while maintaining the CoFe_2O_4 molecular structure. In comparison, the Fe/Co correlation is poorer in EP2, and the Fe/Co ratio in EP2 is no longer 2, suggesting that the coordinated Fe/Co diffusion is less efficient or “frustrated” in this phase. A strong negative correlation is equivalent to strong mutual coordination maintaining a constant sum, suggesting two elements are strongly competing to occupy the same crystalline lattice site. Conversely, a poor correlation between two elements indicates that they occupy different lattice sites, exhibiting weak competition. Table 2 lists the Pearson correlation coefficients among the metal concentrations for all four phases. Positive values indicate positive correlation (+1 for strong positive correlation), and negative values indicate negative correlation (−1 for strong negative correlation). Values close to zero indicate poor correlation (0 for no correlation). Armed with such material insights, we infer that, in CGO, Fe and Co prefer to occupy the Ce site, as Ce is diffusing out of the initial matrix. In EP1, Gd and Ce

Table 2 Linear correlation trends of four metal elements in different phases, estimated using the Pearson correlation coefficients.

	Fe-Co	Fe-Gd	Fe-Ce	Co-Gd	Co-Ce	Gd-Ce
CGO	0.91	NA	-0.97	NA	-0.89	NA
EP1	0.94	-0.62	-0.64	-0.68	-0.55	0.2
EP2	0.69	-0.46	-0.93	-0.82	-0.58	0.16
CFO	0.34	-0.58	NA	-0.91	NA	NA

Strong positive and negative correlations are indicated by bold fonts, while the weak correlations are indicated by italic fonts. The correlations with the elements with a constant concentration are marked as NA (nonapplicable).

show extremely poor correlation, suggesting that they do not compete over the identical crystalline site but prefer different crystalline sites to increase the overall solubilities compensating for their large atomic size. Moderate correlation of Fe and Co with Gd and Ce in EP1 is interpreted that Fe and Co occupy the Gd and Ce sites with comparable probabilities. Similarly, Gd and Ce are highly likely to occupy separate lattice sites in EP2, and there is a high likelihood of Fe/Ce and Co/Gd competitions for occupying the same lattice sites. In CFO, the relative change of atomic ratios of Gd:Co:Fe=4:3:1=1:¾:¼ indicates that, on average, the influx of one Gd atom is compensated by the outflux of ¾ of Co and ¼ of Fe atoms with a higher preference for Gd to occupy the Co site in the CFO crystalline matrix.

Phase transformation mechanism. Based on our findings, we summarize the structural phase transformation in the CGO-CFO MIEC system as follows. During the sintering, a significant amount of Gd and Ce are phase-separated from the initial CGO matrix. The vacancies left by Gd and Ce are efficiently substituted by the highly coordinated influx of Fe and Co from the initial CFO phase, preserving their relative ratio of 2:1. It should be pointed out that Fe has a relatively small solubility (~1%) in CeO₂⁵³. However, it is reasonable to expect that a highly distorted CGO crystal lattice induced by outflux of Gd and Ce could accept much higher concentrations of Fe and Co. The phase-separated Gd and Ce, aided by the highly coordinated Fe/Co diffusion, produce EP1 grains. Compared with CGO grains, the EP1 grains contain significantly higher Gd fractions (35~63%) and lower Ce fractions (8~38%). The formation of EP1 prevents the formation of Gd oxide species, which exhibit poor ionic transport properties. CGO and EP1 have comparable levels of Fe solubility below ~30%. Further incorporation of Fe into the EP1 lattice causes a first-order phase transition to EP2, allowing a maximum Fe solubility of ~52%.

The quantitative 3D fluorescence X-ray imaging analysis unveils crucial material insights that can be exploited for optimizing the functionality of multiphase MIEC systems. For EP1, doping with Fe³⁺/Co²⁺ (ratio 2:1) increases the extrinsic oxygen vacancy concentration in the host and therefore enhances oxygen ion migration. In addition, the metal-oxygen bond energies for Fe-O (407 kJ/mol) and Co-O (397 kJ/mol) are lower compared to that of Ce-O (790 kJ/mol) and Gd-O (715 kJ/mol)⁵⁴, leading to a decreased migration energy E_m and thus enhanced mobility of oxygen. Therefore, the oxygen transport property of EP1 should increase with Fe(Co) concentration. The EP2 phase formed by incorporation of Fe³⁺ from nearby CFO phase into EP1, exhibiting the Fe solubility range from 30% to 52%. Kitchen *et al.* investigated the oxygen vacancy formation energy (ΔE_{vac}) ordering encompassing a broad set of bulk perovskite materials and suggested that the relative energetic trends of the specific

material systems with similar crystal structures will not change⁵⁵. This result can be generalized to energetic trends involving similarly structured metal oxide systems. Particularly for the EP2 phase, the oxygen vacancy formation energy with Co at B-site is always lower than that of Fe at the B-site. Therefore, excessive incorporation of Fe³⁺ into EP2 will hinder the oxygen ion conduction. Incorporation of Fe³⁺ at levels in excess of 36% in EP1 is detrimental to the oxygen transport properties. Ultimately, the excess diffusion of Fe³⁺ into EP1 is due to the high concentration of Fe³⁺ in the parent CoFe₂O₄ phase. Potential methods to preserve the EP1 phase and maintain high oxygen ion transport would be to optimize the parent phase composition with decreased Fe/Co content (i.e., start with a spinel composition of the form Co_{1.5}Fe_{1.5}O₄⁵⁶ or a better combination of two initial parent phases) or to execute finer control of Fe/Co diffusion into the emergent phases. With regard to the conductivity change of the main phase (CGO, Ce_{0.88-3x}Gd_{0.12}Co_xFe_{2x}O_{1.94-2x}), it can be regarded as substitution of Gd with Co and Fe in Ce_{0.8}Gd_{0.2}O_{1.9}. According to the literature⁵⁷, the binding energy of an oxygen vacancy to one or two substitutional cations is a strong function of dopant cation radius, with Gd³⁺ exhibiting the highest ionic conductivity of all doped ceria materials. Because both the radius of Fe³⁺ (0.78 Å) and Co²⁺ (0.79 Å) are smaller than Gd³⁺ (1.053 Å), therefore, the binding energy of oxygen vacancy would increase with doping of Fe³⁺ and Co²⁺, which may lead to a decreased slight decrease in the conductivity of the main phase CGO. However, this is countered by improved interfacial conduction, as outlined below. Nonetheless, the oxygen ionic conduction in dual-phase composite material may also be related to 1) the space charge effect in the grain boundaries of the oxygen ionic conductor (such as CGO), and 2) some extent to the increased tortuosity introduced by the electronic conductive phase. In the case of CGO-CFO composites, even though there is a relatively small amount of emergent phase, i) CGO (51% volume fraction), ii) CFO (34% volume fraction), and iii) EP1 + EP2 (15% volume fraction). It plays an important role in enhancing oxygen conduction. Firstly, the grain boundary conductivity is improved by the formation of EP1 + EP2, keeping a high level of oxygen vacancy concentration along the CGO-CGO grain boundary⁴⁶. Secondly, due to the enhanced electronic pathway, the tortuosity of the electronic conductive phase was decreased. Thirdly, the perovskite-like GFCCO phase possesses a perovskite-like structure and a high level of oxygen vacancies which may provide additional pathways for oxygen ion conduction.

Conclusion

In summary, we successfully developed a highly accurate absorption correction method by considering proper 3D trajectories of the fluorescence photons traversing through the sample to the detector. Our method brings an important breakthrough in quantitative 3D fluorescence X-ray imaging, which can be applied broadly for diverse microscopic investigations from the micro-scale to the nanoscale. The application of our method on the MIEC system revealed 3D visualization of elemental diffusion across grain boundaries, responsible for diverse phase transformations in this material system. A total of 340 individual grains with accurately quantified composition enabled a systematic investigation with an unprecedented level of statistical confidence. The results presented highlight the heterogeneous nature of ostensibly simple “dual-phase” materials systems with implications in a wide range of energy conversion and storage devices relying on contact between functional layers of varying compositions and phase structure. Specifically, in the MIEC system studied in this work, we revealed the formation of two distinct

emergent phases whose composition and spatial distribution are critically important for ensuring excellent transport properties. Furthermore, by developing the mechanistic model for complex phase transformations, we unveil crucial material insights that can be exploited for optimizing the functionality of multiphase MIEC systems. Finally, this work provides a promising path toward the design of high-performance composite MIECs by engineering interfaces: an in-situ phase interaction, which generates new oxygen ion conducting pathways and reduce the space charge effect at the grain boundary simultaneously. This concept could also be applicable to other materials systems, which enables the control of mesoscale level transport property of MIECs.

Methods

Materials synthesis. Commercial CGO ($\text{Ce}_{0.8}\text{Gd}_{0.2}\text{O}_{1.9}$) and CFO (CoFe_2O_4) powders (InfraMat Advanced Materials LLC, USA) with a volume ratio of 60:40 were ball-milled in ethanol for 20 h. Then, they were dried to obtain CGO–CFO composite powders. These powders were pressed into pellets in a 20-mm stainless steel die. The pellets were sintered in air at 1300 °C for two hours. The relative densities of the sintered composites measured by Archimedes' method were all >95%^{45,46}.

Sample preparation. Using a xenon-ion plasma focused-ion beam (PFIB, FEI Helios), a slightly tapered cylindrical sample with a diameter of 6 μm at the top and 8 μm at the bottom was milled from the bulk material and mounted via Pt weld onto a sharp tungsten pin for tomographic imaging⁵⁸.

X-ray fluorescence tomography measurement. The XRF tomography measurements were conducted at the Hard X-ray Nanoprobe (HXN) beamline⁵⁹ of the National Synchrotron Light Source II (NSLS-II). A monochromatic X-ray beam of 12 keV in energy was focused down to a 50 nm spot size using an X-ray zoneplate. Scanning XRF imaging is performed by raster-scanning the sample through the focused beam, and the XRF signals were collected using a three-element Vortex silicon drift detector. In each scan, the data from all three elements are collected simultaneously and are fitted to determine the integrated XRF intensity from the elements (Gd, Fe, Co, and Ce) of interest. Tomography measurements were conducted by collecting a total of 61 2D XRF projection images over a 180° angular range. Each 2D XRF image consists of 160 × 160 pixels with 80 nm pixel size. The elemental maps are produced by fitting the XRF spectra using PyXRF⁶⁰, and TomoPy⁶¹ was used for 3D reconstruction.

Absorption correction. Before applying absorption correction, the 2D elemental maps are normalized by the intensity of the incident X-ray beam. The relative atomic concentration distributions for Gd, Ce, Fe, Co, and Ga (to account for Ga contamination due to FIB) are performed by additional normalization based on their X-ray fluorescence cross-sections. In our analysis, we quantify the relative ratios of elemental concentration among these elements without requiring absolute quantification using XRF standards. The self-absorption correction algorithm is implemented in Matlab. See SI for details on matrix representations used for computation.

Image segmentation. After the absorption correction, image segmentation was conducted using the water-shed algorithm provided in the Matlab toolbox. To perform quantitative composition analysis for the identified 340 grains, we assign the metal concentration values for Gd, Ce, Fe, and Co, by averaging their voxel values within the boundary of each grain particle.

Assignment of quaternary composition. To facilitate convenient comparison of material compositions for different material phases, we assign a quaternary composition, $\text{Gd}_x\text{Ce}_y\text{Fe}_w\text{Co}_z$, where the relative metal fractions are normalized as $x + y + w + z = 1$. Thus, we can write the bulk CGO and the bulk CFO phases as $\text{Gd}_{0.2}\text{Ce}_{0.8}\text{Fe}_0\text{Co}_0$ and $\text{Gd}_0\text{Ce}_0\text{Co}_{1/3}\text{Fe}_{2/3}$, respectively.

Extraction of ternary phase diagram. We extract ternary phase diagrams from the quaternary phase diagram by projecting the 4-dimensional phase space along a direction, joining two apexes. Mathematically, there are six possible ways to generate such projections to produce six unique ternary phase diagrams: Fe–Co–(Gd + Ce), Gd–Ce–(Fe + Co), Ce–Co–(Gd + Fe), Gd–Fe–(Ce + Co), Co–Fe–(Gd + Co), and Gd–Co–(Ce + Fe).

Simulation of ternary phase diagrams. In generating the simulated ternary phase diagram, we first generate a Co distribution by combining the uniform and gaussian probability distribution function to match the data closely. Using the constant and linear parameters, a and b , determined from the linear fitting, we

simulate the relationship between M1 vs. M2 by assigning $[M1] = a_r + b_r[M2]$. The values of a_r and b_r are randomly generated using a gaussian distribution with the mean value of a and b , respectively, over two sigma intervals, where the sigma values are chosen to match the experimental dataset.

XRD measurement. Large single crystal samples were ground and filtered through 10-micron mesh and loaded into a 1-mm Kapton capillary for X-ray powder diffraction (XRD) measurements. XRD data were collected with a photon energy of 52 keV at the X-ray Powder Diffraction (XPD) beamline at NSLS-II. The samples were continuously spun during the measurement with a spin speed of 2 revolutions per second to avoid inaccuracy in XRD quantification due to texture. The diffraction patterns were collected using a two-dimensional Perkin Elmer detector with a pixel size of 75 microns positioned at 1.4 m from the sample. The 2D diffraction patterns were radially integrated using Fit2D software⁶² and scaled to generate standard powder diffraction spectra.

Data availability

All relevant data are available from the corresponding author upon reasonable request.

Code availability

All relevant codes are available from the corresponding author upon reasonable request.

Received: 2 November 2021; Accepted: 17 May 2022;

Published online: 06 June 2022

References

- Mahato, N. et al. Progress in material selection for solid oxide fuel cell technology: A review. *Prog. Mater. Sci.* **72**, 141–337 (2015).
- Kim, S. I. et al. Dense dislocation arrays embedded in grain boundaries for high-performance bulk thermoelectrics. *Science* **348**, 109–114 (2015).
- Lu, K. Stabilizing nanostructures in metals using grain and twin boundary architectures. *Nat. Rev. Mater.* **1**, 16019 (2016).
- Mariano, R. G. et al. Selective increase in CO₂ electroreduction activity at grain-boundary surface terminations. *Science* **358**, 1187–1191 (2017).
- Simons, H. et al. Long-range symmetry breaking in embedded ferroelectrics. *Nat. Mater.* **17**, 814 (2018).
- Zhang, Z. Z. et al. A Self-Forming Composite Electrolyte for Solid-State Sodium Battery with Ultralong Cycle Life. *Adv. Energy Mater.* **7**, 1601196 (2017).
- Huang, X. J. et al. 11 nm hard X-ray focus from a large-aperture multilayer Laue lens. *Sci. Rep.-Uk* **3**, 3562 (2013).
- Li, K. N. et al. Tunable hard x-ray nanofocusing with Fresnel zone plates fabricated using deep etching. *Optica* **7**, 410–416 (2020).
- Yan, H. F. et al. Multimodal hard x-ray imaging with resolution approaching 10 nm for studies in material science. *Nano Futures* **2**, 011001 (2018).
- Da Silva, J. C. et al. Efficient concentration of high-energy x-rays for diffraction-limited imaging resolution. *Optica* **4**, 492–495 (2017).
- Holler, M. et al. High-resolution non-destructive three-dimensional imaging of integrated circuits. *Nature* **543**, 402 (2017).
- Thibault, P. et al. High-resolution scanning x-ray diffraction microscopy. *Science* **321**, 379–382 (2008).
- Hong, Y. S. et al. Hierarchical Defect Engineering for LiCoO₂ through Low-Solubility Trace Element Doping. *Chem.-Us* **6**, 2759–2769 (2020).
- Hill, M. O. et al. Measuring Three-Dimensional Strain and Structural Defects in a Single InGaAs Nanowire Using Coherent X-ray Multiangle Bragg Projection Ptychography. *Nano Lett.* **18**, 811–819 (2018).
- Simons, H. et al. Dark-field X-ray microscopy for multiscale structural characterization. *Nat. Commun.* **6**, 6098 (2015).
- Larson, B. C. et al. Three-dimensional X-ray structural microscopy with submicrometre resolution. *Nature* **415**, 887–890 (2002).
- Sprouster, D. J. et al. Dislocation microstructure and its influence on corrosion behavior in laser additively manufactured 316L stainless steel. *Addit. Manuf.* **47**, 102263 (2021).
- Gill, S. K. et al. Quantitative Nanoscale 3D Imaging of Intergranular Corrosion of 304 Stainless Steel Using Hard X-Ray Nanoprobe. *J. Electrochem. Soc.* **166**, C3320–C3325 (2019).
- Zhang, J. N. et al. Trace doping of multiple elements enables stable battery cycling of LiCoO₂ at 4.6V. *Nat. Energy* **4**, 594–603 (2019).
- Zhao, C. H. et al. Bi-continuous pattern formation in thin films via solid-state interfacial dealloying studied by multimodal characterization. *Mater. Horiz.* **6**, 1991–2002 (2019).

21. Pattammattel, A. et al. High-sensitivity nanoscale chemical imaging with hard x-ray nano-XANES. *Sci. Adv.* **6**, eabb3615 (2020).
22. Victor, T. W. et al. Lanthanide-Binding Tags for 3D X-ray Imaging of Proteins in Cells at Nanoscale Resolution. *J. Am. Chem. Soc.* **142**, 2145–2149 (2020).
23. Hogan, J. P. et al. Fluorescent Computer-Tomography - a Model for Correction of X-Ray Absorption. *IEEE T Nucl. Sci.* **38**, 1721–1727 (1991).
24. Bal, G. & Moireau, P. Fast numerical inversion of the attenuated Radon transform with full and partial measurements. *Inverse. Probl.* **20**, 1137–1164 (2004).
25. Natterer, P. Inversion of the attenuated Radon transform. *Inverse. Probl.* **17**, 113–119 (2001).
26. Golosio, B. et al. Internal elemental microanalysis combining x-ray fluorescence, Compton and transmission tomography. *J. Appl. Phys.* **94**, 145–156 (2003).
27. Schroer, C. G. Reconstructing x-ray fluorescence microtomograms. *Appl. Phys. Lett.* **79**, 1912–1914 (2001).
28. Miqueles, E. X. & De Pierro, A. R. Iterative Reconstruction in X-ray Fluorescence Tomography Based on Radon Inversion. *IEEE T Med. Imaging* **30**, 438–450 (2011).
29. La Riviere, P. J. & Vargas, P. A. Monotonic penalized-likelihood image reconstruction for X-ray fluorescence computed tomography. *IEEE T Med. Imaging* **25**, 1117–1129 (2006).
30. La Riviere, P. J. et al. Penalized-likelihood image reconstruction for x-ray fluorescence computed tomography. *Opt. Eng.* **45**, 077005 (2006).
31. Gursoy, D. et al. Hyperspectral image reconstruction for x-ray fluorescence tomography. *Opt. Express.* **23**, 9014–9023 (2015).
32. Di, Z. W. et al. Joint reconstruction of x-ray fluorescence and transmission tomography. *Opt. Express* **25**, 13107–13124 (2017).
33. Di, Z. C. et al. Optimization-Based Approach for Joint X-Ray Fluorescence and Transmission Tomographic Inversion. *Siam J. Imaging Sci.* **9**, 1–23 (2016).
34. Liu, Y. J. et al. Relating structure and composition with accessibility of a single catalyst particle using correlative 3-dimensional micro-spectroscopy. *Nat. Commun.* **7**, 12634 (2016).
35. Huang, R. et al. Quantitative X-ray fluorescence computed tomography for low-Z samples using an iterative absorption correction algorithm. *Aip. Adv.* **7**, 055111 (2017).
36. Brinkman, K. & Huang, K. Solid Oxide Fuel Cells and Membranes. *Chem. Eng. Prog.* **112**, 44–49 (2016).
37. Shao, Y. Y. et al. Making Li-Air Batteries Rechargeable: Material Challenges. *Adv. Funct. Mater.* **23**, 987–1004 (2013).
38. Bouwmeester, H. J. M. Dense ceramic membranes for methane conversion. *Catal. Today* **82**, 141–150 (2003).
39. Zeng, F. L. et al. Phase and microstructural characterizations for $\text{Ce}_{0.8}\text{Gd}_{0.2}\text{O}_{2-\delta}$ - FeCo_2O_4 dual phase oxygen transport membranes. *J. Eur. Ceram. Soc.* **40**, 5646–5652 (2020).
40. Zeng, F. L. et al. Enhancing oxygen permeation of solid-state reactive sintered $\text{Ce}_{0.8}\text{Gd}_{0.2}\text{O}_{2-\delta}$ - FeCo_2O_4 composite by optimizing the powder preparation method. *J. Membrane Sci.* **628**, 119248 (2021).
41. Fischer, L. et al. Phase formation and performance of solid state reactive sintered $\text{Ce}_{0.8}\text{Gd}_{0.2}\text{O}_{2-\delta}$ - FeCo_2O_4 composites. *J. Mater. Chem. A* **10**, 2412–2420 (2022).
42. He, S. et al. In Situ Formation of $\text{Er}_{0.4}\text{Bi}_{1.6}\text{O}_3$ Protective Layer at Cobaltite Cathode/ Y_2O_3 - ZrO_2 Electrolyte Interface under Solid Oxide Fuel Cell Operation Conditions. *ACS Appl. Mater. Inter.* **10**, 40549–40559 (2018).
43. Lee, K. T. et al. Rational Design of Lower-Temperature Solid Oxide Fuel Cell Cathodes via Nanotailoring of Co-Assembled Composite Structures. *Angew Chem. Int. Edit.* **53**, 13463–13467 (2014).
44. Hong, T. et al. Enhanced Oxygen Reduction Activity on Ruddlesden-Popper Phase Decorated $\text{La}_{0.8}\text{Sr}_{0.2}\text{FeO}_3$ - δ 3D Heterostructured Cathode for Solid Oxide Fuel Cells. *ACS Appl. Mater. Inter.* **9**, 8659–8668 (2017).
45. Harris, W. M. et al. Characterization of 3D interconnected microstructural network in mixed ionic and electronic conducting ceramic composites. *Nanoscale* **6**, 4480–4485 (2014).
46. Lin, Y. et al. Enhancing grain boundary ionic conductivity in mixed ionic-electronic conductors. *Nat. Commun.* **6**, 6824 (2015).
47. Ramasamy, M. et al. Influence of Microstructure and Surface Activation of Dual-Phase Membrane $\text{Ce}_{0.8}\text{Gd}_{0.2}\text{O}_{2-\delta}$ - FeCo_2O_4 on Oxygen Permeation. *J. Am. Ceram. Soc.* **99**, 349–355 (2016).
48. Zvonareva, I. et al. Electrochemistry and energy conversion features of protonic ceramic cells with mixed ionic-electronic electrolytes. *Energ. Environ. Sci.* **15**, 439–465 (2022).
49. Zeng, F. L. et al. Micromechanical Characterization of $\text{Ce}_{0.8}\text{Gd}_{0.2}\text{O}_{2-\delta}$ - FeCo_2O_4 Dual Phase Oxygen Transport Membranes. *Adv Eng Mater* **22**, 1901558 (2020).
50. Natterer, F. Numerical methods in tomography. *Acta. Numerica* **8**, 34 (1999).
51. Grover, V. & Tyagi, A. K. Phase relations, lattice thermal expansion in CeO_2 - Gd_2O_3 system, and stabilization of cubic gadolinia. *Mater. Res. Bull.* **39**, 859–866 (2004).
52. Artini, C. et al. Structural characterization of the $\text{CeO}_2/\text{Gd}_2\text{O}_3$ mixed system by synchrotron X-ray diffraction. *J. Solid State Chem.* **190**, 24–28 (2012).
53. Zhang, T. S. et al. The effect of Fe doping on the sintering behavior of commercial CeO_2 powder. *J. Mater. Process Tech.* **113**, 463–468 (2001).
54. Luo, Y.-R., *Comprehensive handbook of chemical bond energies*. 1st Edition ed; CRC press: 2007.
55. Curnan, M. T. & Kitchin, J. R. Effects of Concentration, Crystal Structure, Magnetism, and Electronic Structure Method on First-Principles Oxygen Vacancy Formation Energy Trends in Perovskites. *J. Phys. Chem. C* **118**, 28776–28790 (2014).
56. Bhowmik, R. N. et al. Synthesis of $\text{Co}_{1.5}\text{Fe}_{1.5}\text{O}_4$ spinel ferrite with high magnetic squareness and study its magnetic property by annealing the chemical routed sample at different temperatures. *J. Alloy Compd.* **559**, 134–141 (2013).
57. Minervini, L. et al. Defect cluster formation in M_2O_3 -doped CeO_2 . *Solid State Ionics* **116**, 339–349 (1999).
58. Lombardo, J. J. et al. Focused ion beam preparation of samples for X-ray nanotomography. *J. Synchrotron Radiat.* **19**, 789–796 (2012).
59. Nazaretski, E. et al. Design and performance of an X-ray scanning microscope at the Hard X-ray Nanoprobe beamline of NSLS-II. *J. Synchrotron Radiat.* **24**, 1113–1119 (2017).
60. Li, L. et al. PyXRF: Python-based X-ray fluorescence analysis package. *Proceedings Volume 10389, X-Ray Nanoimaging: Instruments and Methods III 103890U* (2017).
61. Gursoy, D. et al. TomoPy: a framework for the analysis of synchrotron tomographic data. *J. Synchrotron Radiat.* **21**, 1188–1193 (2014).
62. Hammersley, A. P. et al. Two-dimensional detector software: From real detector to idealised image or two-theta scan. *High Pressure Res.* **14**, 235–248 (1996).

Acknowledgements

The research used the Hard X-ray Nanoprobe (HXN) beamline at 3-ID and the X-ray Powder Diffraction (XPD) beamline at 28-ID-2 of the National Synchrotron Light Source II, a U.S. Department of Energy (DOE) Office of Science User Facility operated for the DOE Office of Science by Brookhaven National Laboratory under Contract No. DE-SC0012704. This research is also partially supported by the Laboratory Directed Research and Development (LDRD 15–037 and LDRD 20–030) program at the Brookhaven National Laboratory. This research used resources of the Advanced Photon Source, a U.S. Department of Energy (DOE) Office of Science User Facility operated for the DOE Office of Science by Argonne National Laboratory under Contract No. DE-AC02-06CH11357. The authors acknowledge financial support from an Energy Frontier Research Center on Science-Based Nano-Structure Design and Synthesis of Heterogeneous Functional Materials for Energy Systems (HeteroFoaM Center) funded by the U.S. Department of Energy, Office of Science, Office of Basic Energy Sciences (Award no. DE-SC0001061).

Author contributions

M.G. and Y.C. designed the research; M.G., X.H., H.Y. S.G. and Y.C. conducted the XRF and XRD measurements; M.G., D.G., J.Z., Y.M., W.C., K.B., and Y.C. analyzed the results; Y.C. supervised the research; M.G. and Y.C. prepared the manuscript.

Competing interests

The authors declare no competing interests.

Additional information

Supplementary information The online version contains supplementary material available at <https://doi.org/10.1038/s43246-022-00259-x>.

Correspondence and requests for materials should be addressed to Yong S. Chu.

Peer review information *Communications Materials* thanks Huaidong Jiang, Changyong Song and Fanlin Zeng for their contribution to the peer review of this work. Primary Handling Editor: Aldo Isidori. Peer reviewer reports are available.

Reprints and permission information is available at <http://www.nature.com/reprints>

Publisher's note Springer Nature remains neutral with regard to jurisdictional claims in published maps and institutional affiliations.



Open Access This article is licensed under a Creative Commons Attribution 4.0 International License, which permits use, sharing, adaptation, distribution and reproduction in any medium or format, as long as you give appropriate credit to the original author(s) and the source, provide a link to the Creative Commons license, and indicate if changes were made. The images or other third party material in this article are included in the article's Creative Commons license, unless indicated otherwise in a credit line to the material. If material is not included in the article's Creative Commons license and your intended use is not permitted by statutory regulation or exceeds the permitted use, you will need to obtain permission directly from the copyright holder. To view a copy of this license, visit <http://creativecommons.org/licenses/by/4.0/>.

© The Author(s) 2022